ADVANCED MATERIALS
www.advmat.de

Controlling the Cavity Structures of Two-Photon-Pumped Perovskite Microlasers

*Wei Zhang, Lan Peng, Jie Liu, Aiwei Tang, Jin-Song Hu, Jiannian Yao, and Yong Sheng Zhao**

Micro-/nanolasers have attracted great attention because of their potential applications ranging from high-throughput sensing to on-chip photonic communication.[1] In recent years, two-photon-pumped (TPP) technology is emerging as an ideal alternative to single-photon for fulfilling nanoscale lasers,[2] in which the gain medium can be excited at red or near-infrared wavelengths without phase-matching requirements, and hence show longer lifetimes and photostabilities.[3] Semiconductor microcrystals with large two-photon-absorption (TPA) cross-section, can provide both a gain medium and a resonant cavity for lasing, which have been widely applied for obtaining TPP upconverted lasers.[4] Unfortunately, most inorganic semiconductors suffer from high trap densities and rapid Auger recombination loss, and almost all organic crystals are subjected to severe bimolecular annihilation and excited-state absorption, both leading to relatively high threshold for TPP lasing.[5]

Organometal halide perovskites (OHPs),[6] with large TPA coefficients and bimolecular radiative efficiency,[7] may overcome aforementioned shortcomings, exhibiting huge potential in light amplification and upconversion.[5,8] Indeed, strong microcavity effects and single-photon driven stimulated emissions have been widely reported in their related crystal microstructures.[9] Very recently, the TPP luminescence and microlaser were also explored and researched preliminary for wavelength upconversion.[7a,10] Among them, the laser only operates within the peculiar microcavity such as Fabry–Pérot (FP) or whispering gallery mode (WGM), which is formed by the smooth end/lateral facets of perovskite microcrystals with regular morphology. Thus, the specific crystal shape is critical for perovskite laser operation because it vastly influences the microcavity structures (FP or WGM).[11] However, the strategy for controlled synthesis of various desired perovskite microcrystals with regular shape for tailoring the microcavity effects still remains limited.

Methylammonium lead bromide/chloride perovskites usually exhibit a cubic unit cell structure with highly symmetrical bonding interactions in three dimensions at room temperature, and thus readily crystallize into a cubic shape.[12] Traditional shape engineering for perovskite crystals by solution-precipitation or vapor-deposition without templates and catalysts,[9] is often difficult to be controlled, which generates large morphological variations and structure defects, rendering the assembly of defined microcavity nanostructures relatively difficult. A possible solution is to use the surfactant micelles as soft templates to modulate the kinetic assembly process in liquid phase for fulfilling the controlled assembly of specific perovskite microcrystals.[13] The template method may allow for the fabrication of different dimensional perovskite nanostructures such as one-dimensional (1D) wires or 2D plates, and therefore help to modulate the microcavity structures for perovskite lasers, especially for the TPP lasing.

Herein, we demonstrate a feasible way to control the microcavity structures of perovskite lasers by finely fabricating different microstructures with the micelle-template strategy. The 1D microwires (MWs) and 2D square microplates (MPs) were synthesized in a controlled way from the induction of two different surfactants, octadecylammonium bromide (OTDB) and dodecylammonium bromide (DODB), respectively. The as-fabricated MWs and MPs exhibit large two-photon excited radiative efficiency, resulting in very low-threshold TPP lasing. Moreover, the different lasing actions from 1D MWs and 2D MPs indeed clarifies a shape-dependent microcavity effects, i.e., 1D function as fine FP resonators while 2D act as effective WGM lasing cavities. Meanwhile, based on the different microcavity effects, single-mode FP or WGM lasing can be obtained by tuning the sizes of the corresponding microstructures. These results of controlling microcavity structures and laser properties by modulating kinetic assembly process for fabricating different microstructures, would provide enlightenment for the development of tailor-made mini-sized devices for photonic integrated circuits.

Methylammonium lead bromide ($MAPbBr_3$, **Figure 1**A) was selected as the model perovskite for constructing and tailoring the lasing microcavity due to its large emissive cross-sections and typical cubic crystal structures.[14] As shown in Figure 1A, the $MAPbBr_3$ has a cubic unit cell structure with high symmetry in three dimensions at room temperature. The isotropy of crystals usually brings about the formation of the symmetrically cubic crystal morphology.[12] From the predicted crystal growth based on Bravais–Friedel–Donnay–Harker (BFDH) law using Materials Studio package (Figure 1B), we can see that the isotropical interactions would facilitate the crystal growth along three directions to form a 3D cubic microstructure rather than wires or plates.[15] Thus, control over the kinetic growth process is essential for synthesizing tailor-made $MAPbBr_3$ microcavity structures.[16]

W. Zhang, J. Liu, Prof. J.-S. Hu, Prof. J. Yao, Prof. Y. S. Zhao
Beijing National Laboratory for Molecular Sciences (BNLMS)
Institute of Chemistry
Chinese Academy of Sciences
Beijing 100190, China
E-mail: yszhao@iccas.ac.cn
L. Peng, Prof. A. W. Tang
School of Science
Beijing Jiaotong University
Beijing 100044, China

DOI: 10.1002/adma.201505927

ADVANCED MATERIALS
www.advmat.de

Materials Views
www.MaterialsViews.com

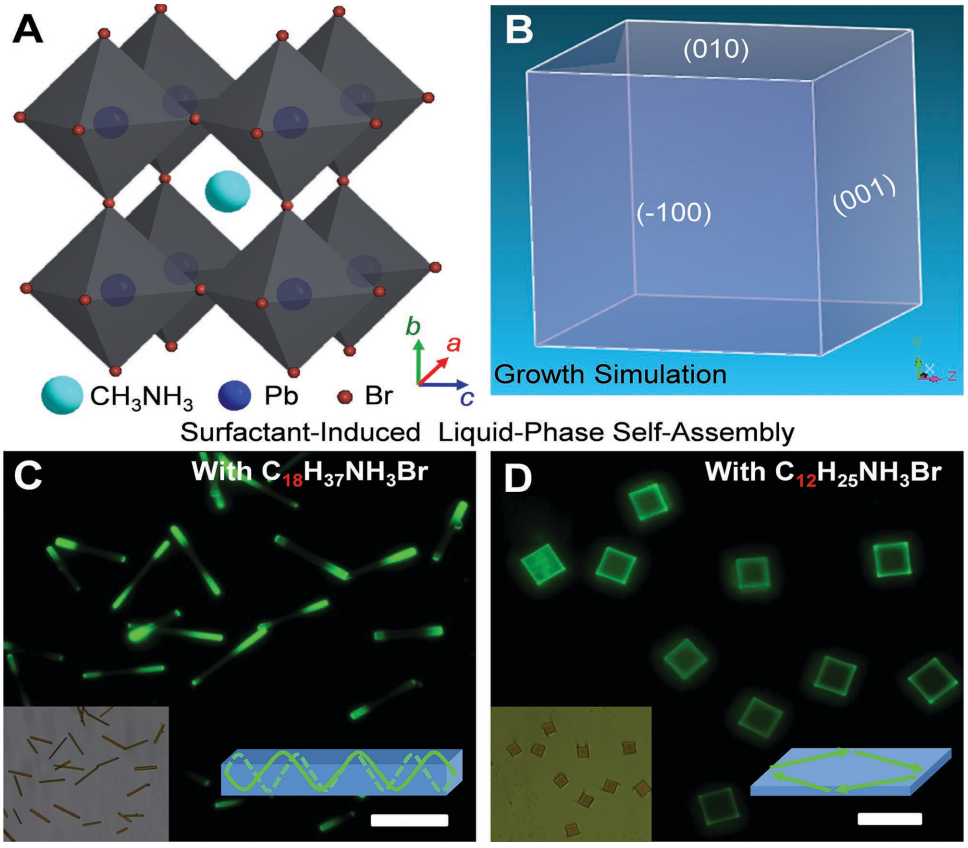

Figure 1. Design and fabrication of perovskite single-crystal microcavity structures. A) The unit-cell structure of the perovskite $MAPbBr_3$. B) Theoretically predicted growth morphology of a $MAPbBr_3$ crystal based on the BFDH theory using Materials Studio package. C,D) PL and bright-field (left insets) images of as-prepared 1D wire-like and 2D plate-like $MAPbBr_3$ microcrystals. The excitation light source is UV band (330–380 nm) of a mercury lamp. All scale bars are 10 μm. Right Insets: schematic depiction of a 1D or a 2D waveguide with cleaved end/lateral facets defining a FP or WGM cavity, respectively.

The $MAPbBr_3$ microstructures were fabricated with a surfactant-assisted liquid-phase self-assembly method (see the Supporting Information).[17] In a typical preparation, a stock solution (30 μL) of $CH_3NH_3Br{\cdot}PbBr_2$ (35 wt%) in *N,N*-dimethylformamide (DMF) was rapidly injected into 1 mL γ-butyrolactone in the presence of surfactants (OTDB or DODB) as soft templates under stirring at room temperature. The change of the dissolubility initiated the nucleation and self-assembly of $MAPbBr_3$. Right after mixing, the colloid solutions were annealed at a constant temperature oven at 60 °C for at least 20 min to remove parts of solvents which would be beneficial for the further aging and assembling of the $MAPbBr_3$ nanocrystals. It is noted that the surfactant templates are very critical for the controlled synthesis of specific perovskite micro-/nanostructures.[13,14,18]

As shown in Figure 1C,D, the OTDB surfactant successfully induced the assembly of 1D wire-like microcrystals while the DODB surfactant mainly initiates the formation of the 2D plate-like square microstructures (also see Figure S2, Supporting Information). The as-prepared MWs exhibit strong green photoluminescence (PL) with bright spots at the wire ends under unfocused UV excitation (Figure 1C), suggesting an axial FP-type microcavity waveguiding characteristic (inset of Figure 1C).[19] In sharp contrast, the PL image of the plates shows bright green light at the four edges and very weak emission from the bodies (Figure 1D), indicating that the square plates can effectively confine and circulate the PL inside the 2D plane, which may be resulted from the WGM resonance waveguiding by the total reflection of four lateral sides (inset of Figure 1D).[20]

The efficient microcavity waveguiding from the wires or plates, can be attributed to the smooth surfaces and defect-free crystal structure, as shown in the scanning electron microscopy (SEM) images in **Figure 2**A,C. The flatness of the surface and the rectangular shape of cross section, are also clearly illustrated in the atomic force microscopy (AFM, Figure S3, Supporting Information). For the chemical composition of the microcrystals, the energy-dispersive X-ray spectroscopy (EDS) analysis presents a N:Pb:Br ratio of about 1:1:3 (Figure S4, Supporting Information), which is in good agreement with a stoichiometry of $CH_3NH_3PbBr_3$ crystal (Figure 1A). Furthermore, the transmission electron microscopy (TEM) images and the corresponding selected area electron diffraction (SAED) patterns in Figure 2B,D indicate that the 1D wire is a high-quality single crystal growing along the [001] direction while the microplate shows distinct 2D single-crystal growing directions that are ascribed to the [110] and [1-10], respectively. It can be seen from the X-ray diffraction (XRD) spectra in Figure 2E that the

DOI: 10.1002/adma.201505927

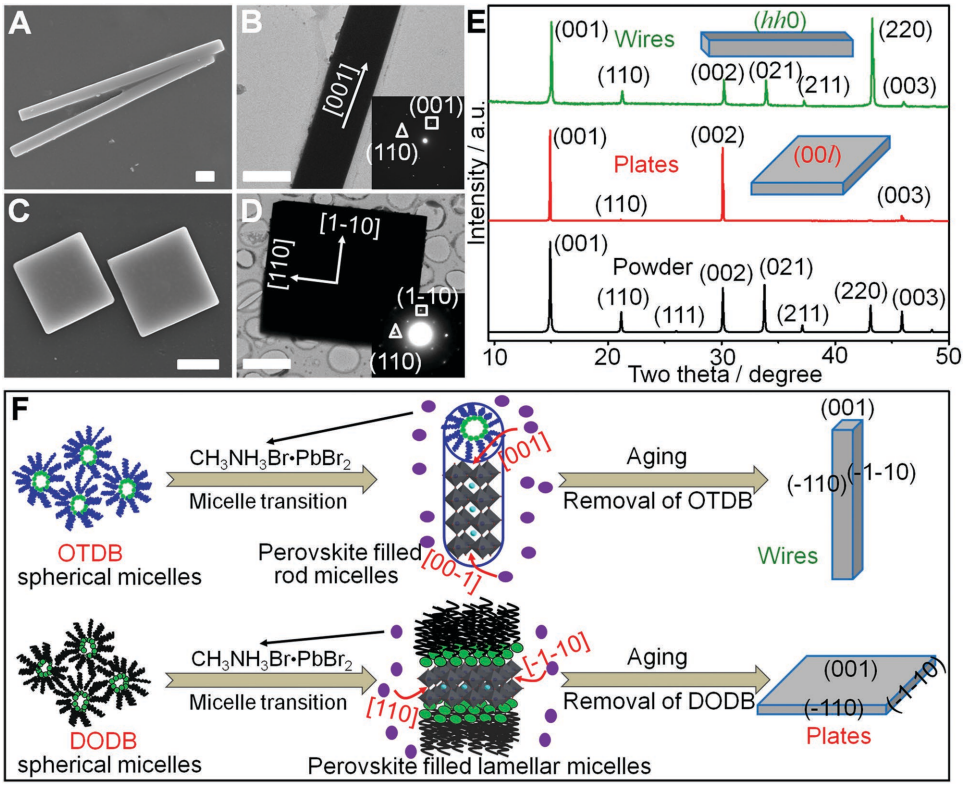

Figure 2. Surfactant-induced assembled mechanism and structure characterization of perovskite microcrystals. A,B) SEM and TEM images of the 1D perovskite $MAPbBr_3$ MWs. Scale bars are 500 nm. Inset: SAED pattern of a single wire. C,D) SEM and TEM images of the 2D square $MAPbBr_3$ MPs. Scale bars are 2 μm. Inset: SAED pattern of a single plate. E) XRD patterns of perovskite $MAPbBr_3$ wires (green), plates (red), and simulated powder pattern using Mercury software (black). Insets: cartoons of a wire and a plate marked with a crystal plane which is parallel to the substrate. F) Schematic illustration for the formation mechanisms of the $MAPbBr_3$ microcrystals.

horizontally placed MWs, compared with the powder, show very strong (*hh*0) diffraction signal peaks, indicating the radial directions of the wires are ascribed to the growth of (110) series of crystal planes. Whereas for the MPs lying on the substrate, the (00*l*) series of diffraction peaks dominate the XRD spectrum, suggesting that the (001) series of crystal planes contribute to the thickness direction growth.[9c]

The results indicate that the shape and size of the finally achieved perovskite microstructures strongly depend on the growth kinetics, especially the relative rate of (001) and (110) crystal facets, which could be effectively modulated by the surfactant micelle templates during the self-assembly in the liquid phase.[13] The growth processes of the two distinct kinds of microcrystals are illustrated in Figure 2F. Under relatively low solution concentration, the alkyl ammonium salts, usually generate the spherical micelles in the absence of additional rod/lamel-inducing reagent.[21] The introduction of $MAPbBr_3$ into the spherical OTDB (or DODB) micelles induced the sphere-to-rod (or sphere-to-lamel) transition of OTDB (or DODB) micelles. The distinct template effects should be resulted from the selective interplay between the surfactants and different crystal facets of $MAPbBr_3$. Because the ammonium cationic head group of the surfactants could strongly coordinate to Br^- ions by hydrogen bonds, the position of the Br^- ions in $[PbBr_6]$ octahedra on the surfaces of $MAPbBr_3$ crystals is very critical for the selective interaction.[13] Based on the analysis for the crystal facet growth, it can be inferred that the OTDB surfactants selectively bind the Br^- ions of (110) or (1–10) crystal facets and thus impede the growth of the two directions. In contrast, the DODB surfactants preferentially bind the Br^- ions of (001) and then suppress the buildup of the direction.

The selective binding of the surfactants can be compared to the monolayer adsorption of molecules onto crystal surfaces. Better binding is expected by distance match in which the spacing of two Br^- ions on specific crystal planes should be equal to the surfactant–surfactant distance of ideal monolayer adsorption.[13] The surfactant–surfactant distance for the DODB is about 0.67 nm,[22] which is very close to the spacing (0.59 nm) of two Br^- ions on (001) planes (Figure 2F). This will lead to an effective adsorption and passivation of (001) while on the perpendicular surfaces, the packing of DODB is assumed to be of less density. Thus, the preferential growth would take place in the [110] or [1–10] direction, and result in the formation of lamellar micelles. By contrast, the larger spacing (0.83 nm) of two Br^- ions on (110) planes may preferentially match the greater surfactant–surfactant distance from OTDB (Figure 2F), leading to preferential growth in the [001] direction and hence the result of rod micelles. The formed rodlike or lamellar micelles would act as templates to further direct the growth of $MAPbBr_3$ single-crystal MWs or MPs, as displayed in Figure 2F.

The single-crystal MWs and MPs exhibit a relatively stronger PL emission and higher quantum yields than the amorphous perovskite films (Figure S5, Supporting Information). This could be attributed to their larger absorption coefficients, lower defect densities and slower auger recombination compared with amorphous films.[5,23] Interestingly, the $MAPbBr_3$ microcrystals, excited by a near-infrared pulse laser beam (900 nm, 150 fs), emits a strong green fluorescence around 545 nm whose PL intensity quadratically depends on the incident energy, indicating that a TPA-based upconverted emission process does occur (Figure S6, Supporting Information). The emission peak exhibits a 6 nm red-shift compared with the single-photon excited PL (Figure S7, Supporting Information), which can be attributed to the emissions from the localized states because of strong band-to-band absorption and photon re-absorption of the emitted light in the interior region.[24] The TPA cross-section of $MAPbBr_3$ microcrystals, is as large as 11 000 GM (where 1 GM = 10^{-50} cm^4 s $photon^{-1}$) around 900 nm (Figure S7, Supporting Information), which is two orders of magnitude larger than those of the commonly reported semiconductor QDs and organic dyes,[25] suggesting that $MAPbBr_3$ microcrystals can function as excellent upconverted gain media.

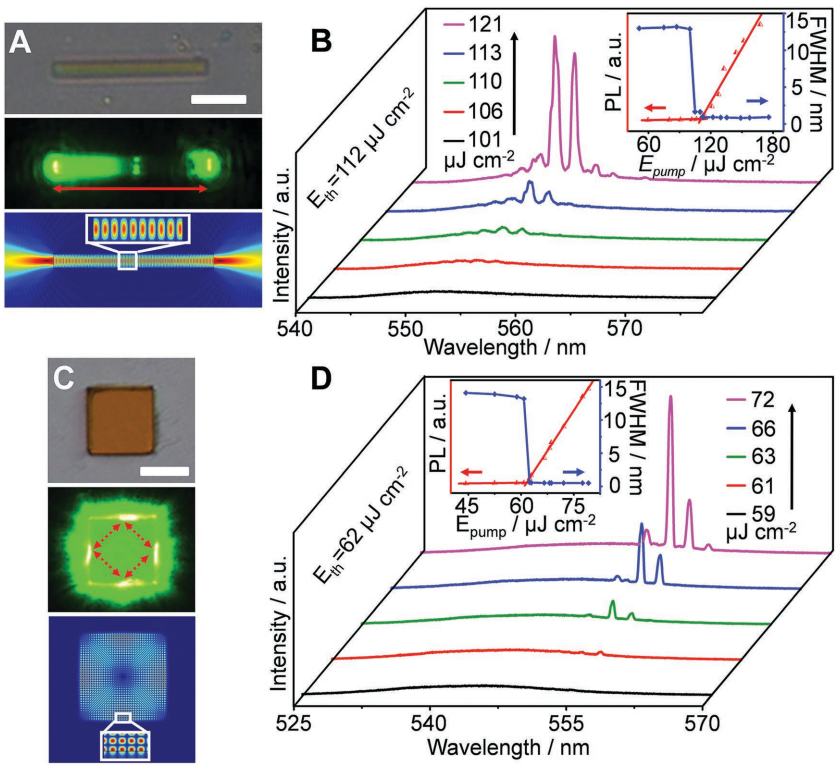

Figure 3. Two-photon pumped perovskite microcavity lasers. A) Bright-field (up) and PL (middle) images of a single wire (L = 13.9 μm) above the thresholds excited uniformly with a pulsed laser (900 nm). Scale bar is 5 μm. Bottom: simulated 2D normalized electric field (λ = 553 nm, n = 2.19), defining a FP standing-wave cavity mode. B) Power-dependent profiles of the PL intensities (red) and FWHM (blue) of the wire around the mode peak 552.9 nm. C) Bright-field (up) and PL (middle) images of a single plate (L = 6.5 μm) above the thresholds excited uniformly with a pulsed laser (900 nm). Scale bar is 5 μm. Bottom: simulated 2D normalized electric field (λ = 552 nm, n = 2.19), showing a WGM travelling-wave cavity mode. D) Power-dependent profiles of PL intensities (red) and FWHM (blue) of the plate around the mode peak 552.3 nm.

When a single $MAPbBr_3$ microwire was pumped uniformly with a near-infrared pulse laser beam (900 nm, 150 fs, Figure S8, Supporting Information), the bright upconverted green emission at the ends of the wire can be observed (**Figure 3**A, middle), indicating a strong TPP axial waveguiding behavior and a typical FP-type microcavity effect (Figure S9, Supporting Information).[26] The FP-type microcavity can support a standing-wave optical field between the two end facets, where the emission would travel back and forth (Figure 3A, bottom), leading to a discrete set of resonant modes in the lasing spectra.[27] As shown in Figure 3B, the FP-type microcavity lasing with a series of mode peaks was obtained in an individual $MAPbBr_3$ microwire (L = 13.9 μm) by increasing the TPP fluence. When the pump fluence arrives to a threshold about 112 μJ cm^{-2}, a strong lasing emerges as a set of sharp mode peaks around 550 nm. Above the onset power, the peak intensity around 552.9 nm increases rapidly and superlinearly with the pump fluence, which reveals a clear knee behavior and a threshold characteristic of a laser (Figure 3B, inset). Furthermore, the full-width at half-maximum (FWHM) at 552.9 nm dramatically narrows down to 0.9 nm with the increase of the TPP fluence, displaying strong microcavity effects with a high quality (Q, defined as λ/FWHM) factor of 600, which is close to the simulated Q factor of 657 (Figure 3A, bottom). This value is pretty high for microwire resonators and can be partially ascribed to the flat end facets that is very essential for axial FP-type microcavity resonance.

In comparison, a single microplate excited uniformly by the same near-infrared pulse laser beam, shows bright upconverted green emission localized at the four edges and weak PL at the body (Figure 3C, middle), which is a characteristic of WGM resonator rather than FP-type microcavity (Figure S9, Supporting Information).[20] The WGM microcavity could sustain a travelling-wave optical field in the 2D plane, in which the emission would be confined by total internal reflection at cavity boundary (Figure 3C, bottom). Therefore, the strong lasing spots occurs on the four edges of the square microplate when the TPP fluence exceeds the threshold of 62 μJ cm^{-2}, as shown in Figure 3C,D. Meanwhile, a set of sharp cavity-mode peaks could be observed in the PL spectra, as displayed in Figure 3D, indicating a distinct 2D WGM lasing. The FWHM at 552.3 nm narrows rapidly from 22 to 0.6 nm with the increasing of the TPP fluence around the onset power, exhibiting a high quality (Q ≈ 920) low-threshold (E_{th} ≈ 62 μJ cm^{-2}) lasing actions (Figure 3D, inset). This Q factor is lower than the simulated value of 2200, which is probably resulted from the shape deformation loss from the square structure.

Adv. Mater. 2016,
DOI: 10.1002/adma.201505927

It is noted that although the TPP thresholds in $MAPbBr_3$ MWs, or MPs lasers are higher than the corresponding single-photon excitation fluences (Figure S10, Supporting Information), they are still markedly lower than conventional inorganic or organic TPP microlasers.[4] This can be mainly attributed to the large TPA coefficients and emissive efficiency. Meanwhile, the high-quality crystal structures such as the smooth surfaces and flat end facets or lateral sides, could also contribute to the low-threshold TPP lasing, because it would well improve the confinement effect of light, and facilitate effective optical microcavity resonance.

The optical microcavity effects of 1D MWs and 2D MPs were further analyzed to investigate the structure–property relationship which would be helpful to modulate the lasing actions. As shown in **Figure 4**A, the lasing spectra of the three different MWs present a decreasing modes number with the reducing of the wire length. The mode spacing ($\Delta\lambda$) versus the wire length (L) is in reasonable agreement with that given by the FP equation $\Delta\lambda = \lambda^2/2Ln_g$,[1] where n_g is the group refractive index as a function of wavelength (λ). On the basis of the linear fitting relationship between $\lambda^2/2\Delta\lambda$ and L, the n_g around 553 nm can be identified with a value of 6.7 (Figure 4B), which is nearly consistent with the group refractive index of lead bromide perovskite microlasers calculated from the reported results,[9c,d] confirming the FP-type longitudinal cavity effects (Figure S11, Supporting Information). However, for 2D MPs, the n_g fitted from the same FP equation between $\lambda^2/2\Delta\lambda$ and the side length (d), is 11.3 around 553 nm which is much larger than the group refractive index of $MAPbBr_3$ microlasers, suggesting that the cavity modes do not result from the FP-type resonance at two parallel edges. By contrast, according to the WGM equation $\Delta\lambda = \lambda^2/n_gL = \lambda^2/n_g2\sqrt{2}d$,[20] the calculated $n_g \approx 7.1$ around 553 nm is very close to the reported group refractive index, which further verifies a four-edge reflected WGM lasing mechanism (Figure S12, Supporting Information).

The very small MWs or MPs can still function as effective FP-type or WGM laser resonators (Figure 4A,C), providing a possibility to obtain single-mode lasers which would help to avoid the temporal pulse broadening and the false signaling in quantum processing and communicating.[28] It is well known that the single-mode lasing could be fulfilled when the mode spacing exceeds the linewidth ($\Delta\lambda \approx 5$ nm, Figure S13, Supporting Information) of the gain region.[29] Based on the FP or WGM microcavity effects (Figure 4B,D), the $\Delta\lambda \approx 5$ nm can be achieved when the wire length decreases to 6 μm, or the plate side length is close to 3.5 μm. By controlling the microcavity sizes (Figure S2, Supporting Information), the single-mode lasers were successfully fulfilled in both 1D MWs ($L = 5.6$ μm) and 2D MPs ($d = 3.1$ μm) (Figure 4A,C).

In summary, the 1D microwires and 2D microplates of lead bromide perovskite have been controllably fabricated by selectively binding two surfactants to different crystal planes, which is essential for modulating the kinetic process of the self-assembly. The as-prepared wires and plates exhibit good crystal quality and large two-photon emission efficiency, resulting in low-threshold TPP lasing. Moreover, the lasing actions from the microwires and microplates demonstrate two kinds of distinct microcavity effects, FP and WGM, respectively. The reported results would help us to fabricate miniaturized lasers with specific functionalities through better understanding the structure–property relations, and to promote the advancement of organic–inorganic hybrid flexible optical elements into miniaturized photonic circuits with higher performances.

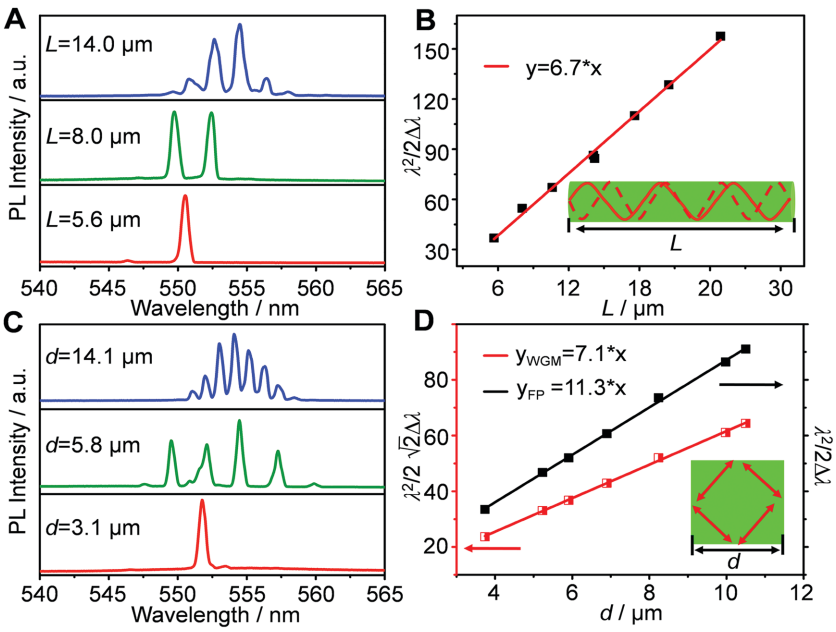

Figure 4. Microcavity modulation of the perovskite lasers. A) Modulated FP-type lasing spectra collected at the guided tips of three $MAPbBr_3$ wires with different lengths (L). B) The plot and fitted curve of $\lambda^2/2\Delta\lambda$ ($\lambda = 553$ nm) versus the length of the wires. C) Modulated WGM lasing spectra collected at the guided tips of three $MAPbBr_3$ square plates with different side-lengths (d). D) The plot and fitted curve of $\lambda^2/2\sqrt{2}\Delta\lambda$ (red) and $\lambda^2/2\Delta\lambda$ (black) ($\lambda = 553$ nm) versus the side-length of the plates.

Experimental Section

Preparation of Perovskite Microcrystals: The $MAPbBr_3$ microstructures were fabricated with a surfactant-assisted liquid-phase self-assembly method (see Figure S1, Supporting Information). In a typical preparation, a stock solution (30 μL) of $CH_3NH_3Br{\cdot}PbBr_2$ (35 wt%) in *N*,*N*-dimethylformamide was rapidly injected into 1 mL of γ-butyrolactone in the presence of surfactants (0.7×10^{-3} M $CH_3(CH_2)_{17}NH_3Br$ or 0.25×10^{-3} M $CH_3(CH_2)_{11}NH_3Br$) as soft templates under stirring at room temperature. The difference of dissolubility in two solvents, which the DMF has better dissolving capacity for the $MAPbBr_3$ than the γ-butyrolactone, would change the surroundings, and thus initiated the nucleation and self-assembly of $MAPbBr_3$. Right after, the mixed colloid solutions were annealed in constant temperature oven at 60 °C for 20 min to remove parts of solvents which would be beneficial for the further aging and assembling of the $CH_3NH_3PbBr_3$ microcrystals, and then the solution was dropped onto the coverslip substrate. Finally the

solvents evaporated, and the microstructures were obtained. It is noted that the surfactants are very critical for the controlled synthesis of specific perovskite microstructures (see Figure S2, Supporting Information). The $CH_3(CH_2)_{17}NH_3Br$ surfactants induces the formation of $MAPbBr_3$ microwires, while the $CH_3(CH_2)_{11}NH_3Br$ mainly directs the assembly of $MAPbBr_3$ microplates. By changing the preparation conditions (e.g., annealed temperature, mother solution concentration, surfactant concentration, and aging time), the (edge) length of the microwires or microplates can be tuned from several to hundreds of microns, and the width or thickness can also be controlled from hundreds of nanometers to several micrometers.

Structural and Morphological Characterization: The morphology and crystallinity of the as-prepared $MAPbBr_3$ microwires or microplates were examined by scanning electron microscopy (SEM) (Hitachi S-4800), transmission electron microscopy (TEM) (JEOL JEM-2010), and atom force microscopy (Vecco Nanoscope IIIa). X-ray diffraction (XRD) (Japan Rigaku D/max-2500) was measured with Cu K_α radiation. Energy-dispersive X-ray spectroscopy (EDX) was performed on single $MAPbBr_3$ microcrystals using a Hitachi S-4800 field-emission scanning electron microscope equipped with an EDS detector operating at 10.0 kV.

Optical Measurements: The fluorescence and diffused reflection absorption spectra were measured with Hitachi F-7000 and Shimidazu UV-2600 spectrophotometers, respectively. The absolute quantum yields were measured by using the Hamamatsu Absolute Quantum Yield Spectrometer C11347. The schematic illustration of the experimental setup for the optical characterization of single microcrystals is shown in Figure S8 in the Supporting Information. PL images and confocal images were taken with an Olympus FluoView-500 inverted microscope. To measure the two-photon excited PL spectra of the single $MAPbBr_3$ microwires or microplates, the samples were excited uniformly with a 900 nm Ti-sapphire laser (150 fs, 1 kHz) focused down to a spot about 15 μm diameter through an objective (Nikon CFLU Plan, 20 ×, N.A. = 0.5). The excitation laser was filtered with a 900 nm band-pass filter. The power at the input was altered by the neutral density filters. The emissions from the single $MAPbBr_3$ microcrystals, which were filtered with a 720 nm short-pass filter, were dispersed with a grating (600 G mm^{-1}) and recorded with a thermal-electrically cooled CCD (Princeton Instruments, ProEm: 1600B).

Supporting Information

Supporting Information is available from the Wiley Online Library or from the author.

Acknowledgements

This work was supported by the National Natural Science Foundation of China (21125315, 21533013, 21521062), the Ministry of Science and Technology of China (2012YQ120060), and the Strategic Priority Research Program of the Chinese Academy of Sciences (XDB12020300).

Received: November 29, 2015
Revised: February 2, 2016
Published online:

[1] a) M. T. Hill, M. C. Gather, *Nat. Photonics* **2014**, *8*, 908; b) M. H. Huang, S. Mao, H. Feick, H. Yan, Y. Wu, H. Kind, E. Weber, R. Russo, P. Yang, *Science* **2001**, *292*, 1897; c) D. O'Carroll, I. Lieberwirth, G. Redmond, *Nat. Nanotechnol.* **2007**, *2*, 180.

[2] a) C. F. Zhang, Z. W. Dong, G. J. You, S. X. Qian, H. Deng, *Opt. Lett.* **2006**, *31*, 3345; b) C. Zhang, F. Zhang, T. Xia, N. Kumar, J.-i. Hahm, J. Liu, Z. L. Wang, J. Xu, *Opt. Express* **2009**, *17*, 7893.

[3] a) G. S. He, P. P. Markowicz, T.-C. Lin, P. N. Prasad, *Nature* **2002**, *415*, 767; b) Q. Zheng, H. Zhu, S. C. Chen, C. Tang, E. Ma, X. Chen, *Nat. Photonics* **2013**, *7*, 234.

[4] a) J. Jiang, Q. Liao, Y. S. Zhao, J. Yao, *J. Mater. Chem.* **2011**, *21*, 4837; b) C. Zhang, C. L. Zou, Y. Yan, R. Hao, F. W. Sun, Z. F. Han, Y. S. Zhao, J. Yao, *J. Am. Chem. Soc.* **2011**, *133*, 7276; c) J. Yu, Y. Cui, H. Xu, Y. Yang, Z. Wang, B. Chen, G. Qian, *Nat. Commun.* **2013**, *4*, 2719.

[5] G. Xing, N. Mathews, S. S. Lim, N. Yantara, X. Liu, D. Sabba, M. Grätzel, S. Mhaisalkar, T. C. Sum, *Nat. Mater.* **2014**, *13*, 476.

[6] a) A. Poglitsch, D. Weber, *J. Chem. Phys.* **1987**, *87*, 6373; b) A. Kojima, K. Teshima, Y. Shirai, T. Miyasaka, *J. Am. Chem. Soc.* **2009**, *131*, 6050.

[7] a) G. Walters, B. R. Sutherland, S. Hoogland, D. Shi, R. Comin, D. P. Sellan, O. M. Bakr, E. H. Sargent, *ACS Nano* **2015**, *9*, 9340; b) M. Saba, M. Cadelano, D. Marongiu, F. Chen, V. Sarritzu, N. Sestu, C. Figus, M. Aresti, R. Piras, A. Geddo Lehmann, C. Cannas, A. Musinu, F. Quochi, A. Mura, G. Bongiovanni, *Nat. Commun.* **2014**, *5*, 5049; c) C. Wehrenfennig, G. E. Eperon, M. B. Johnston, H. J. Snaith, L. M. Herz, *Adv. Mater.* **2014**, *26*, 1584; d) W. Tian, C. Zhao, J. Leng, R. Cui, S. Jin, *J. Am. Chem. Soc.* **2015**, *137*, 12458; e) H.-H. Fang, R. Raissa, M. Abdu-Aguye, S. Adjokatse, G. R. Blake, J. Even, M. A. Loi, *Adv. Funct. Mater.* **2015**, *25*, 2378.

[8] a) F. Deschler, M. Price, S. Pathak, L. E. Klintberg, D.-D. Jarausch, R. Higler, S. Hüttner, T. Leijtens, S. D. Stranks, H. J. Snaith, M. Atatüre, R. T. Phillips, R. H. Friend, *J. Phys. Chem. Lett.* **2014**, *5*, 1421; b) B. R. Sutherland, S. Hoogland, M. M. Adachi, C. T. Wong, E. H. Sargent, *ACS Nano* **2014**, *8*, 10947.

[9] a) Q. Zhang, S. T. Ha, X. Liu, T. C. Sum, Q. Xiong, *Nano Lett.* **2014**, *14*, 5995; b) J. Xing, X. F. Liu, Q. Zhang, S. T. Ha, Y. W. Yuan, C. Shen, T. C. Sum, Q. Xiong, *Nano Lett.* **2015**, *15*, 4571; c) Q. Liao, K. Hu, H. Zhang, X. Wang, J. Yao, H. Fu, *Adv. Mater.* **2015**, *27*, 3405; d) H. Zhu, Y. Fu, F. Meng, X. Wu, Z. Gong, Q. Ding, M. V. Gustafsson, M. T. Trinh, S. Jin, X. Zhu, *Nat. Mater.* **2015**, *14*, 636.

[10] Z. Gu, K. Wang, W. Sun, J. Li, S. Liu, Q. Song, S. Xiao, *Adv. Opt. Mater.* **2016**, *4*, 472.

[11] D. Venkatakrishnarao, R. Chandrasekar, *Adv. Opt. Mater.* **2016**, *4*, 112.

[12] V. Steinmann, R. E. Brandt, T. Buonassisi, *Nat. Photonics* **2015**, *9*, 355.

[13] T. Kollek, D. Gruber, J. Gehring, E. Zimmermann, L. Schmidt-Mende, S. Polarz, *Angew. Chem. Int. Ed.* **2015**, *54*, 1341.

[14] L. C. Schmidt, A. Pertegás, S. González-Carrero, O. Malinkiewicz, S. Agouram, G. Mínguez Espallargas, H. J. Bolink, R. E. Galian, J. Pérez-Prieto, *J. Am. Chem. Soc.* **2014**, *136*, 850.

[15] D. Winn, M. F. Doherty, *AIChE J.* **2000**, *46*, 1348.

[16] a) Y. Yan, Y. S. Zhao, *Chem. Soc. Rev.* **2014**, *43*, 4325; b) P. Tyagi, S. M. Arveson, W. A. Tisdale, *J. Phys. Chem. Lett.* **2015**, *6*, 1911.

[17] C. Zhang, Y. Yan, Y. S. Zhao, J. Yao, *Acc. Chem. Res.* **2014**, *47*, 3448.

[18] a) F. Zhu, L. Men, Y. Guo, Q. Zhu, U. Bhattacharjee, P. M. Goodwin, J. W. Petrich, E. A. Smith, J. Vela, *ACS Nano* **2015**, *9*, 2948; b) F. Zhang, H. Zhong, C. Chen, X.-g. Wu, X. Hu, H. Huang, J. Han, B. Zou, Y. Dong, *ACS Nano* **2015**, *9*, 4533.

[19] a) W. Zhang, Y. Yan, J. Gu, J. Yao, Y. S. Zhao, *Angew. Chem. Int. Ed.* **2015**, *54*, 7125; b) Y. S. Zhao, P. Zhan, J. Kim, C. Sun, J. Huang, *ACS Nano* **2010**, *4*, 1630.

[20] H. H. Fang, R. Ding, S. Y. Lu, Y. D. Yang, Q. D. Chen, J. Feng, Y. Z. Huang, H. B. Sun, *Laser Photonics Rev.* **2013**, *7*, 281.

[21] Y. Lei, Q. Liao, H. Fu, J. Yao, *J. Am. Chem. Soc.* **2010**, *132*, 1742.
[22] H. Heinz, R. Vaia, R. Krishnamoorti, B. Farmer, *Chem. Mater.* **2007**, *19*, 59.
[23] a) S. M. Vorpahl, S. D. Stranks, H. Nagaoka, G. E. Eperon, M. E. Ziffer, H. J. Snaith, D. S. Ginger, *Science* **2015**, *348*, 683; b) S. D. Stranks, V. M. Burlakov, T. Leijtens, J. M. Ball, A. Goriely, H. J. Snaith, *Phys. Rev. Applied Appl.* **2014**, *2*, 034007.
[24] Y. Yamada, T. Yamada, L. Q. Phuong, N. Maruyama, H. Nishimura, A. Wakamiya, Y. Murata, Y. Kanemitsu, *J. Am. Chem. Soc.* **2015**, *137*, 10456.
[25] S. C. Pu, M. J. Yang, C. C. Hsu, C. W. Lai, C. C. Hsieh, S. H. Lin, Y. M. Cheng, P. T. Chou, *Small* **2006**, *2*, 1308.
[26] L. K. Van Vugt, B. Piccione, C.-H. Cho, P. Nukala, R. Agarwal, *Proc. Natl. Acad. Sci. USA* **2011**, *108*, 10050.
[27] I. D. W. Samuel, E. B. Namdas, G. A. Turnbull, *Nat. Photonics* **2009**, *3*, 546.
[28] a) H. Gao, A. Fu, S. C. Andrews, P. Yang, *Proc. Natl. Acad. Sci. USA* **2013**, *110*, 865; b) L. Feng, Z. J. Wong, R. M. Ma, Y. Wang, X. Zhang, *Science* **2014**, *346*, 972.
[29] R. Chen, V. D. Ta, H. D. Sun, *Sci. Rep.* **2012**, *2*, 244.